RSC Advances

PAPER

View Article Online
View Journal | View Issue

Cite this: *RSC Adv.*, 2017, **7**, 55691

Pr^{3+} doped tellurite glasses incorporated with silver nanoparticles for laser illumination

Chenxiao Hua,[ab] Xin Zhao,[a] Edwin Yue Bun Pun[b] and Hai Lin *[ab]

Received 20th October 2017
Accepted 23rd November 2017

DOI: 10.1039/c7ra11594f

rsc.li/rsc-advances

Enhanced red fluorescence emissions of Pr^{3+} were observed in heavy metal germanium tellurite (HGT) glasses containing silver nanoparticles (NPs). The well-dispersed Ag NPs with a diameter ~7 nm were evidenced by transmission electron microscope (TEM). With the introduction of Ag NPs, multichannel transition emission intensity of Pr^{3+} increased by ~25% in comparison with that in the case without silver doping, which is attributed to the existence of the localized surface plasmon resonance (LSPR) referring to the characteristic absorption peaks. The larger the net emission power, the higher was the net emission photon number and the higher quantum yield in Pr^{3+} doped HGT glasses containing Ag NPs, presenting the effectiveness of utilizing laser. An efficient fluorescence emission and macroscopical sensitization illustrate that the Pr^{3+}-doped HGT glasses with Ag NPs are potential materials, which improve the color-rendering index for laser illumination.

1. Introduction

In the past decades, nanometer-sized particles of metals have attracted increasing attention due to several tempting properties such as optical nonlinearity, thermal characteristics, and magnetic properties,[1–4] which are different from their bulk states. In recent years, considerable attention has been paid to the photometric characteristics of the noble metal (usually silver and gold) nanoparticles, which are embedded in a glass host accompanying with rare-earth (RE) ions, thus effectively boosting the fluorescence of rare-earth ions.[5–7] Silver nanoparticles (NPs) function as an ideal sensitizer, which could enhance the emission efficiency of rare-earth ions due to the influence of the localized surface plasmon resonance (LSPR).[8–10] The combination of RE ions and silver NPs provides a hopeful direction in the fabrication of optical devices for laser illumination.[11–15]

Among oxide glass systems, tellurite glasses show a compromise between the demand for a proper chemical durability and the desire for a low cut-off phonon energy, which is ideal for the device fabrication and rare-earth fluorescence.[16–24] With the introduction of germanium ions, the distribution of phonon energy changes and thus the density of the maximum phonons is reduced. In addition, the Pr^{3+} doped tellurite glasses with multichannel emissions have been considered as a prospective candidate for the adjustment of color rendering index in laser applications.[25–27] Furthermore, the tellurite glass host provides a feasible method to synthesize silver NPs by the addition of AgCl and further heat-treatment process, which is promising to achieve a luminescence enhancement of Pr^{3+} in the tellurite glasses with the presence of Ag NPs.[28–30] Moreover, although the ostensible fluorescence enhancement has been reported, the internal macroscopical sensitization under an excitation of the blue laser with a high power in the tellurite glasses containing Ag NPs is seldom reported, which is more meaningful for further understanding the enhancement of fluorescence behavior when silver nanoparticles are added and expands the scope of the application of the optoelectronic devices containing Ag NPs.[31–34]

In this study, the Pr^{3+} doped heavy metal germanium tellurite glasses containing Ag NPs were fabricated by a melt-quenching method with a post-annealing treatment and the existence of Ag NPs was further observed by transmission electron microscopy. The multichannel transition emission of Pr^{3+} increased by ~25% in the Ag NPs embedded glasses compared with that in the silver-free glasses and the intense red fluorescence emissions were captured in the glass samples under the excitation of the short-wavelength visible lights, which are generated from the emitting $^3P_0$ and $^1D_2$ levels of Pr^{3+}, and can be used as the excitation lights for minimally invasive PDT treatment. The absolute characterization of the glass samples containing Ag NPs under the excitation of a 453 nm blue laser was carried out and the high quantum yields were derived from the absolute spectral parameters, thus proving a macroscopical sensitization with a high-power laser. An efficient fluorescence emission and megascopic sensibilization in the Pr^{3+} doped HGT glasses with Ag NPs under the laser excitation provide a promising orientation to develop the efficient optical devices and a tunable red fluorescence is an important support for laser illumination in improving the color-rendering index.

[a]*School of Textile and Material Engineering, Dalian Polytechnic University, Dalian 116034, P. R. China. E-mail: lhai@dlpu.edu.cn*

[b]*Department of Electronic Engineering and State Key Laboratory of Millimeter Waves, City University of Hong Kong, Tat Chee Avenue, Kowloon, Hong Kong, P. R. China*

2. Experiments

Pr^{3+}-doped heavy metal germanium tellurite glasses (HGT) were prepared from high purity Na_2CO_3, Bi_2O_3, PbO, GeO_2, TeO_2, $Pr(NO_3)_3 \cdot 6H_2O$, and AgCl powders according to the molar host composition $2Na_2O$–$17Bi_2O_3$–$2PbO$–$19GeO_2$–$60TeO_2$ with an additional $x$wt% $Pr(NO_3)_3$ and $y$wt% AgCl, where $x = 0.22$ and $y = 0$ was labeled as HGT-Pr and $x = 0.22$ and $y = 0.5$ was marked HGT-PrAH. The raw materials were well-ground in an agate mortar, heated in a pure alumina crucible to 880 °C and maintained at this temperature for 20 min and then quenched onto an aluminum plate. Furthermore, the glasses were subsequently annealed at 320 °C for 2 h to eliminate an internal stress and then cooled down to room temperature slowly. The HGT-PrAH glass containing silver was then heat-treated at 350 °C for 2 h and cooled down to room temperature slowly. For the optical measurements, the glass samples were sliced and polished into pieces with two parallel sides.

The densities of the HGT-Pr and HGT-PrAH glass samples were measured to be 6.106 and 6.110 g cm^{-3}, respectively, and the number densities of Pr^{3+} were calculated to be 2.469×10^{19} and 2.461×10^{19} cm^{-3}, respectively. Using a Metricon 2010 prism coupler, the refractive indices of the HGT-Pr and HGT-PrAH glass samples were measured to be 2.1053 and 2.1062 at 635.96 nm and 2.0431 and 2.0456 at 1546.9 nm, respectively. In addition, the refractive indices at other wavelengths can be calculated by Cauchy's equation $n = A + B/\lambda^2$, giving $A = 2.0304$ and $B = 30\ 273$ nm^2 for HGT-Pr glass and $A' = 2.0333$ and $B' = 29\ 495$ nm^2 for HGT-PrAH glass.

The absorption spectra were recorded using a Perkin Elmer UV-VIS-NIR Lambda 750 spectrophotometer. The visible fluorescence spectra were measured by a Hitachi F-7000 fluorescence spectrophotometer. Differential scanning calorimetry (DSC) was conducted using an American TA company SDT 600 at the rate of 10 °C min^{-1} from room temperature to 1000 °C under a N_2 atmosphere. A 200 kV JEM-2100 transmission electron microscope (TEM), which functioned with selected area electron diffraction (SAED), was used to investigate the nucleation of Ag NPs formed in the glasses. The specimens for TEM images were prepared by dispersing the ground glass powder in ethanol using an ultrasonic bath. The spectral power distributions of the glass samples were measured using an integrating sphere (Labsphere) with a 3.3 inch diameter, which was connected to a CCD detector (Ocean Optics, QE65000) with 600 μm-core optical fiber and a 453 nm laser pigtailed with 400 μm-core fiber was used as the pump source. All of the above measurements were carried out at room temperature.

3. Results and discussion

3.1. Formation of silver nanoparticles

As shown in Fig. 1, the glass transition temperature (T_g) and crystallization onset temperature (T_x) of the Pr^{3+} doped HGT-PrAH glass with Ag nanoparticles, which were measured by DSC, are 320 °C and 402 °C, respectively.

The Pr^{3+} doped heavy metal germanium tellurite glasses containing Ag NPs are visually transparent and homogeneous

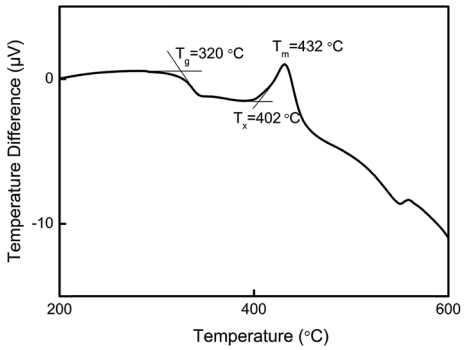

Fig. 1 DSC of the Pr^{3+} doped HGT-PrAH glass with Ag nanoparticles.

as shown in Fig. 2(a). Fig. 2(b), which present the transmission electron microscopy (TEM) images of HGT-PrAH glass sample with the addition of Ag element under different magnifications. As observed from the images, the Ag particles with various sizes and shapes are obtained in the HGT-PrAH glass, which was heat-treated at 350 °C for 2 h. The refined details of the HGT-PrAH glass are investigated by adopting a larger magnification (50 nm, as shown in Fig. 2(c)), which illustrates the generation of Ag NPs with diameters about ~7 nm in the HGT-PrAH glass. To confirm the nucleation of Ag NPs, the selected area electron diffraction (SAED) pattern was recorded (Fig. 2(d)), in which the white spots in the first, second, and third rings originated from the (111), (200), and (220) crystal plane reflections of metallic Ag NPs, respectively, directly proving the presence of metallic Ag in the HGT-PrAH glass.[35,36]

It is worth noting that the formation of Ag^0 NPs from Ag^+ particles occurs through two representative reactions during the high-temperature melting process[37]

$$Ag^+ + e^- \rightarrow Ag^0,\ Ag^+ + Ag^+ \rightarrow Ag^{2+} + Ag^0. \quad (1)$$

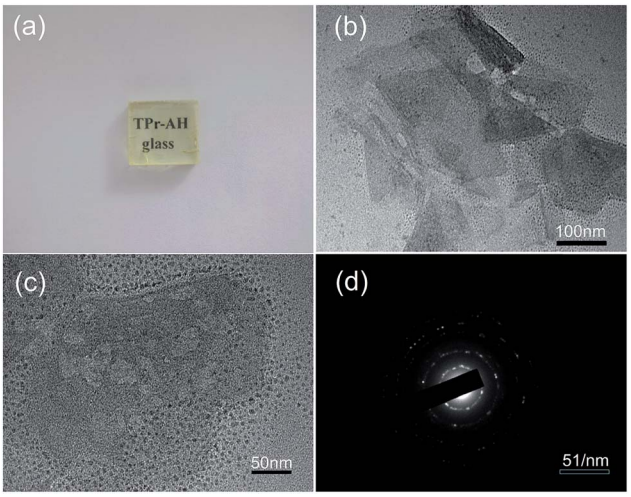

Fig. 2 (a) Photograph of the HGT-PrAH glass with Ag nanoparticles under natural light. (b and c) TEM images of the HGT-PrAH glass with the scale bars of 100 nm and 50 nm. (d) The selected area electron diffraction pattern of HGT-PrAH glass.

Furthermore, a probable mechanism of a selective thermochemical reduction from Ag^{+} ions to Ag^{0} atoms by Te^{4+} ions in the tellurite glasses is considered due to the electromotive force values or reduction potentials of the respective redox system elements, that is[38]

$$Ag^{+}/Ag^{0} = 0.799\ V,\ Te^{6+}/Te^{4+} = 1.02\ V. \quad (2)$$

According to the above reduction processes, following process is likely to occur

$$Te^{4+} + 2Ag^{+} \rightarrow Te^{6+} + 2Ag^{0},\ \Delta E^{0} = +0.578\ V, \quad (3)$$

where ΔE^{0} is the total potential of the reduction process. The viable reaction is eqn (3) (with $\Delta E^{0} > 0$), which illustrates the presence of Ag NPs in the glass system. In addition, it is noteworthy that there is a fraction of Ag particles that can still be present as Ag^{+} ions, atoms, and multimers in the glass samples.[39–42]

3.2. Luminescence properties

Pr^{3+} possesses a variety of radiative transitions from $^{3}P_{0}$ and $^{1}D_{2}$ levels when excited by blue light. With the introduction of Ag NPs, it is promising to enhance the emissions of Pr^{3+}. To experimentally reflect the effects of Ag NPs on the luminescent properties of Pr^{3+} in the glasses, the HGT-Pr and HGT-PrAH glass samples are ground and polished and then the emission spectra are compared under the same excitation conditions as shown in Fig. 3. Five emission bands located at 486, 530, 602, 613, and 646 nm corresponding to $^{3}P_{0} \rightarrow {}^{3}H_{4}$, $^{3}P_{0} \rightarrow {}^{3}H_{5}$, $^{1}D_{2} \rightarrow {}^{3}H_{4}$, $^{3}P_{0} \rightarrow {}^{3}H_{6}$, and $^{3}P_{0} \rightarrow {}^{3}F_{2}$ transitions of Pr^{3+} are observed under a 448 nm radiation.[43–46] Compared to the HGT-Pr glass, in the HGT-PrAH glass, there is a visible increment up to ~25% in the emission intensities. The Pr^{3+} doped heavy metal germanium tellurite glasses exhibit a red fluorescence under the excitation of 448 nm and the fluorescent difference for the HGT-Pr and HGT-PrAH glass samples are shown in the inset photos (I) and (II) of Fig. 3, respectively. It is evident that the fluorescence of HGT-PrAH is brighter than that of the HGT-Pr glass sample, forcefully demonstrating that the characteristic emission from Pr^{3+} is intensified by introducing metallic Ag NPs in the HGT-PrAH glass.

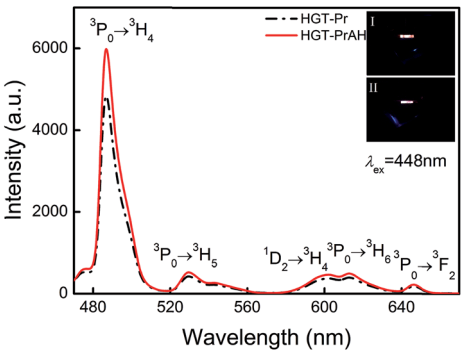

Fig. 3 Emission spectra of the HGT-Pr and HGT-PrAH glasses under a 448 nm excitation. Inset: fluorescence photos (I) and (II) of the HGT-Pr and HGT-PrAH glasses, respectively, under the excitation of 448 nm.

The excitation spectra of the HGT-Pr and HGT-PrAH glass samples monitored at 595 and 646 nm are presented in Fig. 4(a) and (b), respectively. Three excitation bands peaking at 448, 474, and 487 nm are assigned to the absorption transitions of $^{3}H_{4} \rightarrow {}^{3}P_{2}$, $^{3}H_{4} \rightarrow ({}^{1}I_{6}, {}^{3}P_{1})$, and $^{3}H_{4} \rightarrow {}^{3}P_{0}$, respectively, indicating that the emissions originating from the emitting $^{3}P_{0}$ and $^{1}D_{2}$ states can be achieved under the excitation of a commercial blue laser diode, blue and blue-greenish LEDs, and an Ar^{+} optical laser. In addition, under the blue light excitation, the emissions from two levels of Pr^{3+} are clearly enhanced in the HGT-PrAH glass compared to those in the HGT-Pr glass. The excitation band peaking at 595 nm is recorded for a 599 nm emission, which is due to the contribution of $^{1}D_{2} \rightarrow {}^{3}H_{4}$ emission when the $^{1}D_{2}$ level undergoes excitation.

The stimulated emission cross-section σ_{em} is an important parameter to evaluate the energy extraction efficiency of the optical material. From the experimental fluorescence spectra, the σ_{em} for the transition emissions of Pr^{3+} can be evaluated by the Fuchtbauer–Ladenburg (FL) formula:[47]

$$\sigma_{em} = \frac{A_{ij}}{8\pi c n^{2}} \frac{\lambda^{5} I(\lambda)}{\int \lambda I(\lambda) d\lambda}, \quad (4)$$

where n, A_{ij}, $I(\lambda)$, and c represent a refractive index, spontaneous emission probability, fluorescence intensity, and vacuum light velocity, respectively. The obtained σ_{em} profiles of the Pr^{3+} doped heavy metal germanium tellurite glasses in the visible region are shown in Fig. 4(c) and (d) and the peak values (σ_{em}) for $^{1}D_{2} \rightarrow {}^{3}H_{4}$, $^{3}P_{0} \rightarrow {}^{3}H_{6}$, and $^{3}P_{0} \rightarrow {}^{3}F_{2}$ are calculated to be 3.35×10^{-21}, 13.20×10^{-21}, and 89.88×10^{-21} cm^{2}, respectively, for the HGT-Pr glass sample. Furthermore, the corresponding peak values (σ_{em}) of the HGT-PrAH glass are calculated to be 3.57×10^{-21}, 13.99×10^{-21}, and 90.21×10^{-21} cm^{2}, respectively. Although the approximations used in Judd–Ofelt theory gives the predictions that can be off by 20% or more, the efficiency evaluation still can provide the relatively comparable results. The large emission cross-sections for the emission transitions indicate that the intense fluorescence in the 580–660 nm region can be realized in the Pr^{3+}-doped heavy metal germanium tellurite glasses under appropriate excitation conditions. By contrast with the HGT-Pr glass sample, the HGT-PrAH glass with metallic silver NPs possesses larger values on the emission cross-section, indicating that the great red lights derived from the Pr^{3+} ions are promising to improve the color-rendering index in laser illumination. To illustrate the luminescence intensification of the HGT-PrAH glass with Ag NPs, two possible mechanisms of fluorescence enhancement are believed to exist in the HGT-PrAH glass with Ag NPs. The first mechanism is based on the local field enhancement around rare-earth ions and the second is based on the transmission of energy from Ag particles to rare-earth ions. Owing to the fact that spectral shape of the excitation curve has not changed dramatically, the process of energy transmission between Ag NPs and Pr^{3+} is non-dominant in the HGT-PrAH glass. The multichannel luminescence increment of Pr^{3+} is primarily

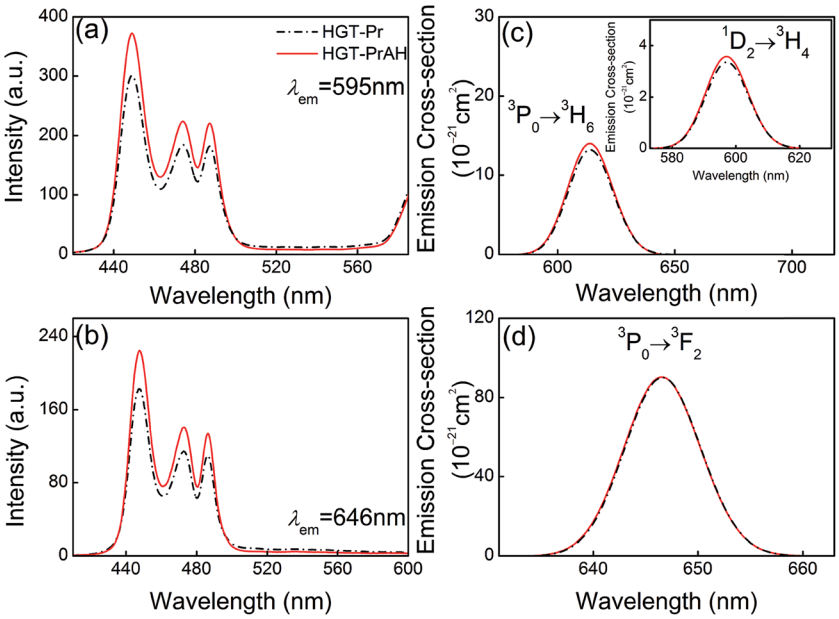

Fig. 4 (a and b) Excitation spectra of the HGT-Pr and HGT-PrAH glasses monitored at 595 and 646 nm. (c and d) Emission cross-section profiles of the HGT-Pr and HGT-PrAH glasses for $^1D_2 \rightarrow {}^3H_4$, $^3P_0 \rightarrow {}^3H_6$, and $^3P_0 \rightarrow {}^3F_2$ transition emissions.

perceived as the local field enhancement around Pr^{3+} induced by Ag NPs in the glass matrix.[48] Thus, when the optical frequency of the incident light beam is approximately near the localized surface plasmon resonance (LSPR) of nanoparticles, a significant luminescence enhancement can be obtained.

3.3. Localized surface plasmon resonance investigation

The measured UV/Vis/NIR absorption spectra of the HGT-Pr and HGT-PrAH glass samples are presented in Fig. 5(a) and (b), which show nine absorption bands peaking at 446, 472, 486, 595, 1009, 1445, 1539, 1939, and 2287 nm associated with the absorption transitions from the ground state $^3H_4$ to the specific excited states. The major absorption peaks are almost uniform in different glass samples except for the slight differences in their intensity when the Ag NPs are introduced. As shown in Fig. 5, the absorbance of the HGT-PrAH glass containing Ag NPs is lower than that of the HGT-Pr glass, which is caused by the existence of a "metallic bridge" for the lead-containing glasses. Metallic Ag and a metallic bridge of Pb easily undergo metallic bonding and the "metallic bridge" of $1/2Pb^0$ exists in Glass–O^{2-}–$1/2Pb^{4+}$–$1/2Pb^0$–Ag–$1/2Pb^0$–$1/2Pb^{4+}$–O^{2-}–Glass, illustrating that metal Ag is highly dispersed in the glasses, which improves the body color and transparency, thus reducing the absorption. Because the LSPR usually hides in the absorption spectra, in order to clearly illustrate the existence of the LSPR, the difference between the absorption coefficients of the HGT-Pr and HGT-PrAH glass samples is presented in the inset of Fig. 5(b), in which the weak LSPR absorption band emerging from 500 to 530 nm is observed. On the basis of Mie theory, the peak of the LSPR absorption band is strongly dependent upon the refractive index of the glass host as follows:[49]

$$\lambda_{max}{}^2 = (2\pi c)^2 m N e^2 (\varepsilon_\infty + 2n^2)/\varepsilon_0, \quad (5)$$

where c is the speed of light, N is the concentration of free electrons, m is the effective mass of the conduction electrons, ε_0 is the permeability of free space, ε_∞ is the optical dielectric function of the metal, and n is the refractive index of the glass. It can be indicated from eqn (5) that the peak wavelength of the LSPR band is in connection with the refractive index of the glasses and the dielectric function of Ag NPs and the classic location of the LSPR absorption lie around the (approximately)

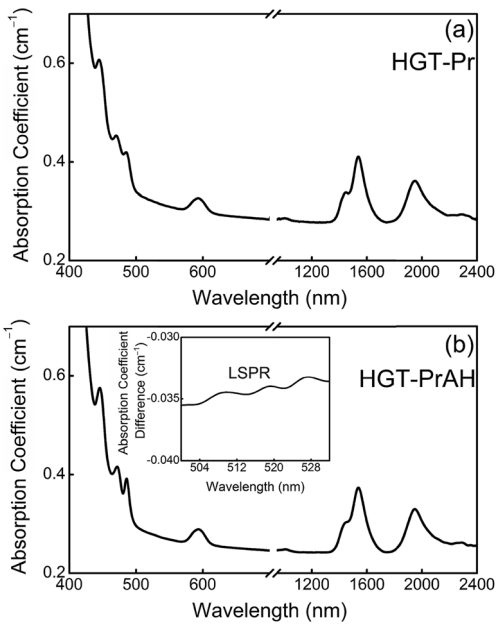

Fig. 5 (a and b) Absorption spectra of HGT-Pr and HGT-PrAH glass samples. Inset: LSPR band of Ag NPs was observed in the HGT-PrAH glass.

410 nm range for the silicate glasses with a refractive index of ~1.5. For the as-obtained HGT glasses, the refractive index is around ~2.2 and the LSPR band should red-shift to a longer wavelength position in comparison with that in the silicate glasses, which is in agreement with the result of the weak LSPR band measured.[50–52]

According to the Judd–Ofelt theory, the radiative transitions belonging to the $4f^2$ configuration of Pr^{3+} can be analyzed based on the absorption of Pr^{3+}. The Judd–Ofelt intensity parameters Ω_t ($t = 2$, 4, and 6) for Pr^{3+} in the HGT-PrAH glass are derived by a least square fitting approach to be 2.07×10^{-20}, 3.23×10^{-20}, and 3.56×10^{-20} cm^2, respectively.[53–55] The intensity parameter Ω_2 has been identified to be sensitive to the asymmetry and the covalency of the rare-earth ions and Ω_4 and Ω_6 are related to the bulk property and rigidity of the samples, respectively. In the HGT-PrAH glass system, Ω_2 is larger than the value of 2.05×10^{-20} cm^2 in the HGT-Pr glass system without Ag NPs, which shows a strong asymmetrical and higher covalent environment owing to the introduction of Ag NPs changing the ligand field of Pr^{3+}, thus achieving the intense fluorescence emission. Using these intensity parameters, some important radiative properties including spontaneous emission probabilities (A_{rad}), luminescence branching ratios (β), and radiative lifetime (τ_{rad}) for the optical transitions of Pr^{3+} in the HGT-Pr and HGT-PrAH glasses are calculated and listed in Table 1. The predicated spontaneous emission probabilities A_{rad} for the transitions $^3P_0 \rightarrow {}^3F_2$, $^3P_0 \rightarrow {}^3H_6$, and $^1D_2 \rightarrow {}^3H_4$ are derived to be 15 570, 7355, and 1503 s^{-1}, respectively, and the relevant branching ratios β account for 23.3%, 11.0%, and 30.5%, respectively, presenting that the emissions of Pr^{3+} in the tellurite glasses are effective.

The luminescence decay curves of the $^3P_0$ and $^1D_2$ levels for the HGT-Pr and HGT-PrAH glasses are shown in Fig. 6(a) and (d). The fluorescent lifetimes (τ_{exp}) of the $^3P_0$ and $^1D_2$ levels can be derived from the fluorescence decays by the following formula:[56]

$$\tau_{exp} = \frac{\int_0^\infty tI(t)dt}{\int_0^\infty I(t)dt}, \quad (6)$$

where $I(t)$ is the emission intensity at time t. The experimental lifetimes (τ_{exp}) of the $^3P_0$ and $^1D_2$ levels for the HGT-Pr and HGT-PrAH glasses are calculated to be 8.65, 8.71, 66.14, and 67.29 μs, respectively. The energy transfer from the Ag species to the RE ions is represented by an apparent increase in lifetime of the emitting RE level and the energy transfer from Ag NPs to the RE ions is not operative since the lifetime of plasma oscillation of Ag particle (10^{-14} s) is much smaller than that of the RE ions (10^{-6} to 10^{-3} s). Thus, the result of the single exponential fitting for the decay curves leads to an increase in the lifetime when silver nanoparticles are added. The quantum efficiency (η_q) of the HGT-Pr and HGT-PrAH glasses are calculated to be 57.71% and 67.89% at the $^3P_0$ level and 32.64% and 34.44% at the $^1D_2$ level, respectively, by using the following equation:

$$\eta_q = \tau_{exp}/\tau_{rad}, \quad (7)$$

where τ_{exp} is the experimental lifetime, which is derived by fitting the fluorescence decay curves for the $^3P_0 \rightarrow {}^1D_2$ and $^1D_2 \rightarrow {}^1G_4$ transition emissions, and the τ_{rad} is the radiative lifetime, which is obtained from Judd–Ofelt analysis. With the introduction of Ag NPs, the quantum efficiency of the $^3P_0$ and $^1D_2$ levels are increased by ~10.18% and ~1.80%, respectively, and the increments of the quantum efficiencies from HGT-Pr to HGT-PrAH glasses occur due to the existence of the LSPR.

3.4. Absolute spectral parameters of the Pr^{3+} doped HGT glasses

An integrating sphere coupled with a pumping laser was applied to measure an absolute spectral parameter, which provides an external quantum yield to evaluate the luminescence materials. The net spectral power distributions of fluorescence for the

Table 1 Predicted spontaneous emission probabilities A_{rad}, branching ratios β, and radiative lifetime τ_{rad} of the Pr^{3+} doped HGT glasses with and without metallic Ag nanoparticles

	HGT-Pr				HGT-PrAH			
Transition	Energy (cm^{-1})	A_{rad} (s^{-1})	β (%)	τ_{rad} (μs)	Energy (cm^{-1})	A_{rad} (s^{-1})	β (%)	τ_{rad} (μs)
$^3P_0 \rightarrow {}^1D_2$	3748	8.91	0.001	14.99	3748	9.04	0.001	12.83
$^3P_0 \rightarrow {}^1G_4$	10 701	1053.91	1.580		10 701	1100.87	1.583	
$^3P_0 \rightarrow {}^3F_4$	14 019	7069.07	10.595		14 021	7378.86	10.612	
$^3P_0 \rightarrow {}^3F_3$	14 119	0.00	0.000		14 126	0.00	0.000	
$^3P_0 \rightarrow {}^3F_2$	15 469	15 570.15	23.340		15 465	15 732.04	23.354	
$^3P_0 \rightarrow {}^3H_6$	16 224	7354.87	11.033		16 229	7820.40	11.092	
$^3P_0 \rightarrow {}^3H_5$	18 450	0.00	0.000		18 450	0.00	0.000	
$^3P_0 \rightarrow {}^3H_4$	20 577	35 661.93	53.451		20 577	37 090.74	53.358	
$^1D_2 \rightarrow {}^1G_4$	6953	519.10	10.516	202.61	6953	534.57	10.444	195.37
$^1D_2 \rightarrow {}^3F_4$	10 271	1552.05	31.441		10 272	1577.07	30.811	
$^1D_2 \rightarrow {}^3F_3$	10 371	164.66	3.336		10 378	169.56	3.313	
$^1D_2 \rightarrow {}^3F_2$	11 721	594.01	12.033		11 717	617.81	12.070	
$^1D_2 \rightarrow {}^3H_6$	12 476	571.93	11.586		12 480	598.69	11.697	
$^1D_2 \rightarrow {}^3H_5$	14 702	31.37	0.635		14 702	32.82	0.641	
$^1D_2 \rightarrow {}^3H_4$	16 829	1503.23	30.453		16 829	1587.97	31.024	

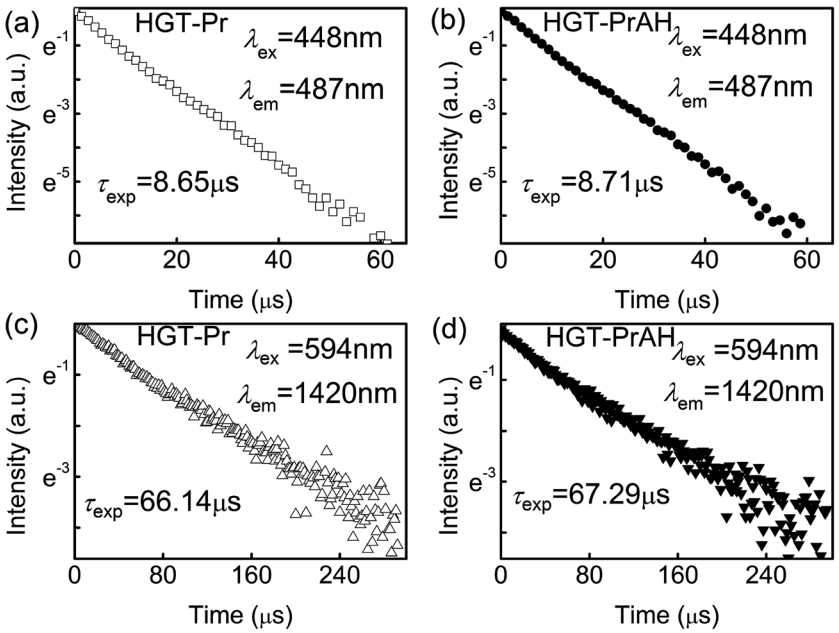

Fig. 6 (a and b) Fluorescence decay curves of the $^3P_0$ level for the HGT-Pr and HGT-PrAH glasses. (c and d) Fluorescence decay curves of the $^1D_2$ level for the HGT-Pr and HGT-PrAH glasses.

HGT-Pr and HGT-PrAH glasses were captured under the excitation of the 453 nm blue laser with various pump powers and presented in Fig. 7. The intense red emission is observed in the Pr^{3+} doped HGT glasses under the excitation of the blue laser as shown in the photographs in Fig. 7. Each spectral power distribution curve comprises seven emission bands in the red and near-infrared region located at 646, 688, 709, 732, 815, 869, and 1038 nm, which are assigned to $^3P_0 \rightarrow {}^3F_2$, $^1D_2 \rightarrow {}^3H_5$, $^3P_0 \rightarrow {}^3F_3$, $^3P_0 \rightarrow {}^3F_4$, $^1D_2 \rightarrow {}^3H_6$, $^1D_2 \rightarrow {}^3F_2$, and $^1D_2 \rightarrow {}^3F_4$ transitions, respectively. Under the excitation of the 453 nm laser with a power (P_{laser}) of 5.13 and 15.02 mW, the net emission spectral powers for the HGT-Pr glass are obtained to 106.08 and 535.17 μW, respectively, and as high as 180.80 and 615.03 μW for the HGT-PrAH glass, respectively, confirming that the metallic Ag NPs doping HGT glasses are conducive to more efficiently utilize laser due to the LSPR of Ag nanoparticles.

According to the net spectral power distribution, the $^3P_0$ and $^1D_2$ levels of Pr^{3+} were sensitized by introducing metallic Ag NPs

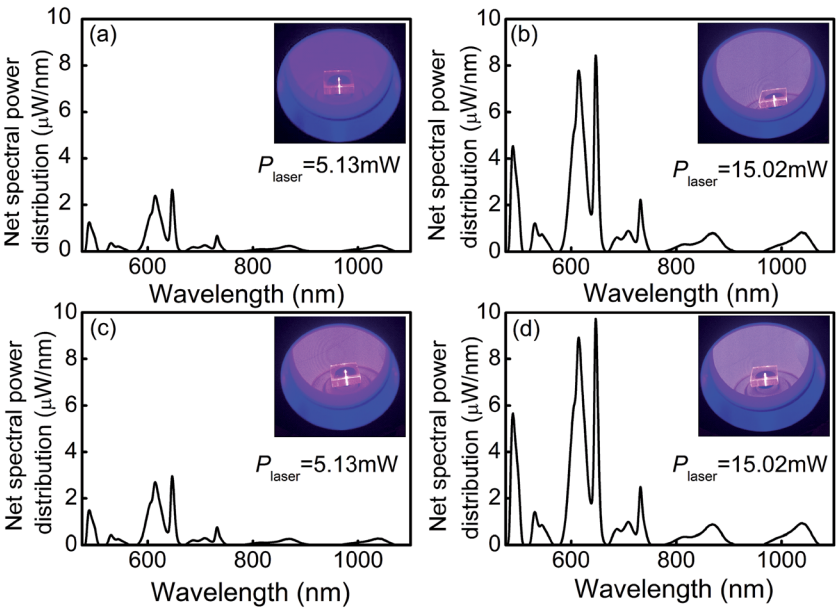

Fig. 7 Net spectral power distribution in HGT-Pr (a and b) and HGT-PrAH (c and d) glasses under the 453 nm laser excitation. Inset: fluorescence photographs of HGT-Pr and HGT-PrAH glasses under the excitation of the 453 nm laser in an integrating sphere.

in the Pr^{3+} doped HGT glasses. Table 2 demonstrates the tangible enhancement in the $^3P_0$ and $^1D_2$ levels under the 453 nm blue laser excitation for diverse powers, implying the sensitized difference of the disparate primary state level. With the increment of the laser power, the enhanced percentage shows an upward trend, indicating that the macroscopical sensitization can be realized under the excitation of the 453 nm blue laser.

Based on the net spectral power distributions of the Pr^{3+} doped HGT glass samples, the photon distributions can be derived from

$$N(\nu) = \frac{\lambda^3}{hc} P(\lambda), \quad (8)$$

where λ is the wavelength, ν is the wavenumber, h is the Planck constant, c is the vacuum velocity of light, and $P(\lambda)$ is the spectral power distribution. Under the 453 nm blue laser excitation for diverse powers, the net absorption and emission photon distribution curves of the Pr^{3+} doped HGT glass samples with metallic Ag NPs are derived from eqn (8) with $P(\lambda)$ as shown in Fig. 8. With the increment of the laser pump power, the emission photon numbers exhibit an antrorse trend for the Pr^{3+} and Ag NPs doped HGT glass samples.

The quantum yield (QY) of the luminescence material is defined as the ratio of the number of photons emitted to those absorbed, which is used as a selection criterion of the luminescence materials for potential applications in solid-state lighting devices.[57] The equation is expressed as follows:

$$QY = N_{em}/N_{abs}. \quad (9)$$

Through this formula, the total QYs of the Pr^{3+} doped HGT glasses with and without Ag NPs under the excitation of the 453 nm blue laser with diverse powers are derived and listed in Table 3. The total QYs of the HGT-Pr and HGT-PrAH glasses are calculated to be 10.95% and 11.84% in the case of 5.13 mW pumping and 11.63% and 11.94% in the case of 15.02 mW pumping, respectively. Under the excitation of the 453 nm laser with the 5.13 mW power, the quantum yield of the HGT-PrAH glass with Ag NPs reaches 11.84%, which is higher than that in the HGT-Pr glass without Ag NPs, suggesting that the macroscopical sensitization is due to the LSPR. Higher photon release efficiency further implies the potential of the Pr^{3+} doped HGT glasses containing Ag NPs for laser illumination.

In order to comprehend the mechanism of the observed luminescence enhancement, the partial energy band diagram for Pr^{3+} in the vicinity of Ag NP is illustrated in Fig. 9. Under the excitation of 448 nm, initially, the $^3P_2$ level is populated by the single-step ground state absorption, accompanying a sequence of non-radiative relaxation that populates the $^3P_0$ state.[58] Following this, the transitions occur from $^3P_0$ to $^3H_4$, $^3H_5$, and $^3F_2$ levels, emitting a series of fluorescence. Moreover, the $^3P_0$ level depopulates non-radiatively through multiphonon-assisted decays to the $^1D_2$ state and then jumps to the $^3H_4$ and $^3H_5$ levels. The emission rates of the Pr^{3+} ions located in the vicinity of Ag NPs increase and the major reason of increment in the emission rates is the mismatch of dielectric constants between the metal and the surroundings due to LSPR. Another approach to further enhancements can be described by an energy transfer (ET) from the surface of Ag NP to Pr^{3+} ion, which plays a secondary role.

3.5. Color anticipation of the Pr^{3+} doped germanium tellurite glass phosphor

For the practicality aspect, the intense red light with an adequate intensity and good directivity in the Pr^{3+} doped HGT glasses provide advantageous surroundings in developing a laser illumination device. Fig. 10 displays the fluorescence photographs corresponding to the HGT-Pr and HGT-PrAH glasses with a long-path laser under the laser excitation. In addition, the fluorescence color diversification can be observed under the excitation of the 453 nm blue laser with diverse powers, demonstrating the notable tunability of color fluorescence of the Pr^{3+} emissions when the laser power increases from 5.13 to 15.02 mW. Moreover, there is a visible aggrandizement with regard to the brightness for the Pr^{3+} doped HGT glasses with Ag NPs under the same excitation condition, suggesting

Table 2 Multiple sensitizations of the $^3P_0$ and $^1D_2$ levels in the Pr^{3+} doped HGT glasses with and without metallic Ag NPs under the 453 nm laser excitation

	5.13 mW pumping			15.02 mW pumping		
	Emission power (μW)			Emission power (μW)		
Transition	HGT-Pr	HGT-PrAH	Enhanced percentage	HGT-Pr	HGT-PrAH	Enhanced percentage
$^3P_0 \rightarrow {}^3F_4$	0.678	0.754	11.21%	2.226	2.493	11.99%
$^3P_0 \rightarrow {}^3F_3$	0.268	0.298	11.19%	0.887	0.984	10.94%
$^3P_0 \rightarrow {}^3F_2$	2.648	2.961	11.82%	8.433	9.732	15.40%
$^3P_0 \rightarrow {}^3H_6$	2.386	2.698	13.08%	7.782	8.919	14.61%
$^3P_0 \rightarrow {}^3H_5$	0.361	0.421	16.62%	1.212	1.410	16.34%
$^3P_0 \rightarrow {}^3H_4$	1.239	1.483	19.69%	4.540	5.659	24.65%
$^1D_2 \rightarrow {}^3F_4$	0.252	0.276	9.52%	0.821	0.928	13.03%
$^1D_2 \rightarrow {}^3F_2$	0.240	0.264	10.00%	0.792	0.881	11.24%
$^1D_2 \rightarrow {}^3H_6$	0.096	0.106	10.42%	0.320	0.351	9.69%
$^1D_2 \rightarrow {}^3H_5$	0.188	0.205	9.04%	0.618	0.680	10.03%
$^1D_2 \rightarrow {}^3H_4$	1.477	1.714	16.05%	4.877	5.705	16.98%

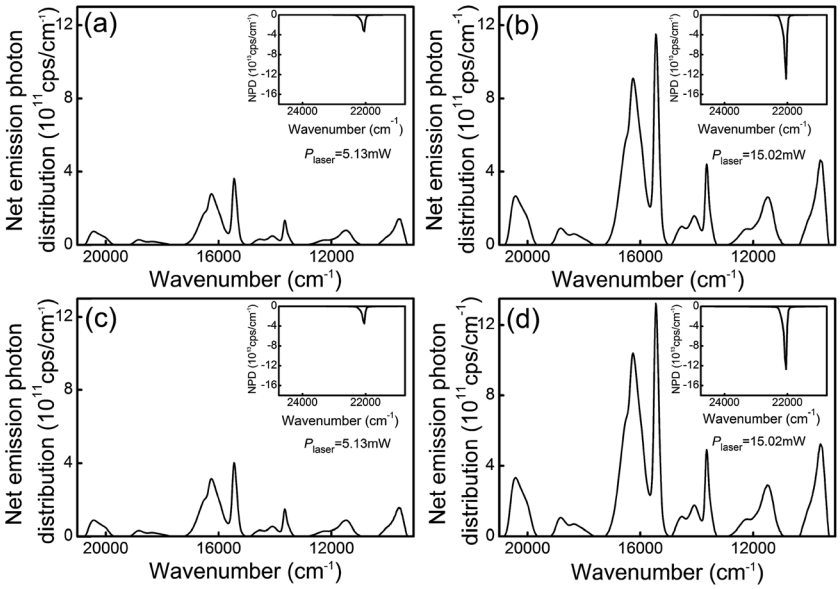

Fig. 8 Net emission photon distributions of the HGT-Pr (a and b) and HGT-PrAH (c and d) glasses under the 453 nm laser excitation. Inset: details of the related net absorption photon distribution.

Table 3 Absorption and emission photon numbers and quantum yield in the Pr^{3+} doped HGT glasses with and without metallic Ag NPs under the 453 nm laser excitation

	5.13 mW pumping		15.02 mW pumping	
	Photon numbers (10^{14} cps)		Photon numbers (10^{14} cps)	
Transition	HGT-Pr	HGT-PrAH	HGT-Pr	HGT-PrAH
Net absorption	48.88	50.95	153.22	170.56
Net emission	5.35	6.03	17.82	20.36
$^3P_0 \rightarrow {}^3H_4$	0.43	0.51	1.62	2.04
$^3P_0 \rightarrow {}^3H_5$	0.21	0.24	0.72	0.82
$^3P_0 \rightarrow {}^3H_6$	2.08	2.37	6.87	7.87
$^3P_0 \rightarrow {}^3F_2$	0.75	0.84	2.45	2.76
$^3P_0 \rightarrow {}^3F_3$	0.19	0.21	0.62	0.68
$^3P_0 \rightarrow {}^3F_4$	0.26	0.29	0.86	0.96
$^1D_2 \rightarrow {}^3H_6$	0.24	0.26	0.78	0.86
$^1D_2 \rightarrow {}^3F_2$	0.38	0.42	1.27	1.39
$^1D_2 \rightarrow {}^3F_4$	0.68	0.75	2.20	2.51
$^1D_2 \rightarrow {}^3H_5$	0.13	0.14	0.43	0.47
Total quantum yield	10.95%	11.84%	11.63%	11.94%

the macroscopical sensitization and providing a potential development in laser illumination devices.

The color coordinates of the colorful fluorescence in HGT-PrAH glasses under the diverse excitation conditions are derived and marked on the CIE-1931 standard chromaticity diagram. A multicolor integral fluorescence derived from the combination of the residual laser and the Pr^{3+} spontaneous emission can be realized by adjusting the intensity ratio between the laser and the Pr^{3+} emissions as shown in Fig. 11.

The CIE 1931 color coordinates for the white fluorescence of the Pr^{3+} doped germanium tellurite glasses under different excitation conditions are calculated using the following formula

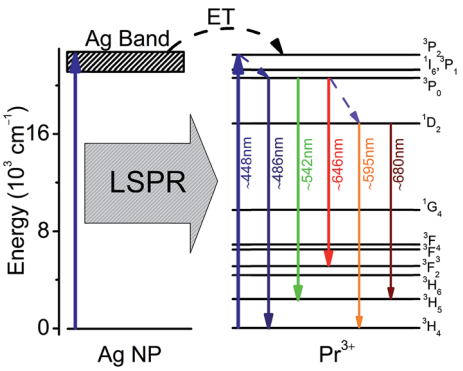

Fig. 9 Energy level diagram of the Pr^{3+} doped HGT glasses in the vicinity of Ag NP.

$$x = \frac{X}{X+Y+Z},\quad y = \frac{Y}{X+Y+Z},\quad z = \frac{Z}{X+Y+Z}, \tag{10}$$

where X, Y, Z are three tristimulus values. The tristimulus values for a color with a spectral power distribution $P(\lambda)$ are acquired by the following:

$$X = \int_{380}^{780} P(\lambda)\bar{x}(\lambda)\mathrm{d}\lambda,\quad Y = \int_{380}^{780} P(\lambda)\bar{y}(\lambda)\mathrm{d}\lambda,\quad Z = \int_{380}^{780} P(\lambda)\bar{z}(\lambda)\mathrm{d}\lambda, \tag{11}$$

where λ is the wavelength of the equivalent monochromatic light and $\bar{x}(\lambda)$, $\bar{y}(\lambda)$, and $\bar{z}(\lambda)$ are three color-matching functions. On varying the intensity ratios between the residual laser and the Pr^{3+} emissions, the color coordinates move along the top left direction to the left boundary of the red region, passing through beneath the pure white region; the nearest-white region is point 3, whose color coordinate is derived to be (0.395, 0.225). White light would be achieved in HGT-PrAH glasses with the assistance of Tb^{3+}, which emits a green fluorescence, which is

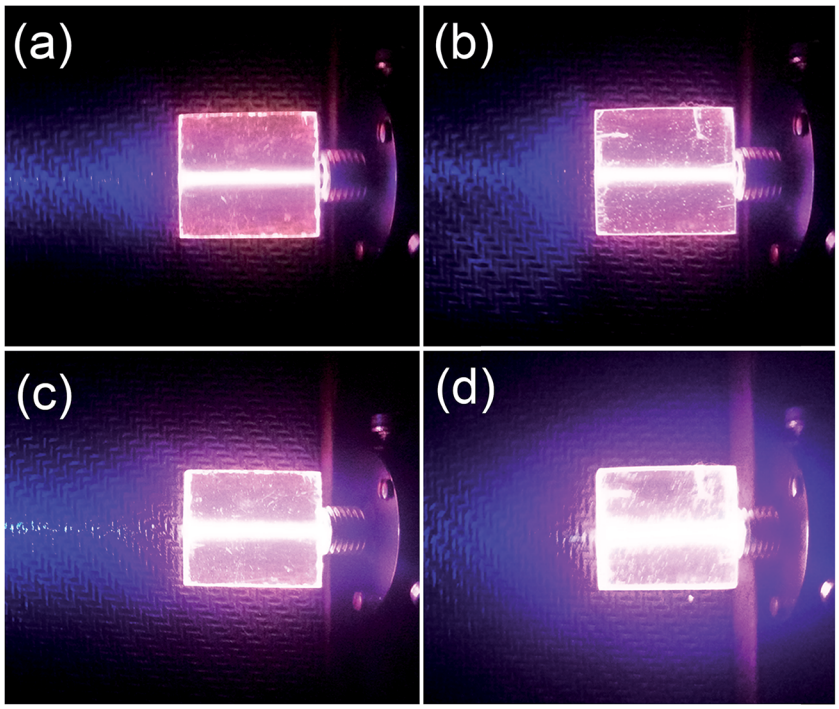

Fig. 10 Fluorescence photographs of (a) HGT-Pr and (b) HGT-PrAH glasses under the 453 nm laser excitation with a power of 5.13 mW. Fluorescence photographs of HGT-Pr (c) and HGT-PrAH (d) glasses under the 453 nm laser excitation with a power of 15.02 mW.

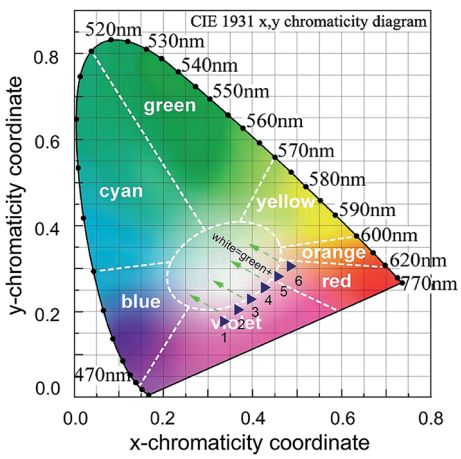

Fig. 11 Color coordinates in the CIE 1931 chromaticity diagrams for HGT-PrAH glasses under the 453 nm laser excitation.

beneficial to the white illumination. Moreover, the Pr^{3+} doped tellurite glasses have also been confirmed as promising materials for light emitting diodes with an additional Er^{3+} ion doping.[59,60] On the whole, the Pr^{3+} doped tellurite glass is an up-and-coming material for the region of the illumination.

4. Conclusions

The Pr^{3+} doped heavy metal germanium tellurite glasses (HGT) containing AgCl was prepared to produce Ag nanoparticles with diameters ~7 nm, which were evidenced by TEM images. The localized surface plasmon resonance (LSPR) band of around 500–530 nm in the prepared glass samples was demonstrated by the absorption spectra. The multichannel transition emission intensity of the Pr^{3+} with Ag NPs embedded HGT-PrAH glasses increased by ~25% in comparison with that in a silver-free glass sample, which illustrates the existence of the LSPR combined the absorption spectra, thus emitting a noticeable red fluorescence. Net emission power and net emission photon number are calculated to be 615.03 μW and 20.37×10^{14} cps, respectively, and the quantum yield is as high as 11.94% in the Pr^{3+} doped HGT glasses with Ag NPs under the excitation of a 453 nm blue laser with a 15.02 mW power. An intense and tunable red fluorescence was observed, demonstrating macroscopical sensitization with the addition of Ag NPs. Furthermore, white light would be achieved by the addition of a green component when the residual laser and the Pr^{3+} emission reach an appropriate range. Moreover, the Pr^{3+} doped tellurite glasses can be applied to light emitting diodes on co-doping with Er^{3+}. The results indicate that the Pr^{3+}-doped HGT glasses with Ag NPs are an exploitable material, which provides an efficient red fluorescence in the improvement of the color-rendering index for laser illumination.

Conflicts of interest

There are no conflicts to declare.

Acknowledgements

The research work was supported by the Natural Science Foundation of Liaoning Province, China (2015020179,

2015020187), and the Research Grants Council of Hong Kong (AOE/P-02/12).

References

1 H. Fares, H. Elhouichet, B. Gelloz and M. Ferid, *J. Appl. Phys.*, 2015, **117**, 205.
2 J. J. Li, R. F. Wei, X. Y. Liu and H. Guo, *Opt. Express*, 2012, **20**, 10122.
3 Z. Yin, X. R. Zhang, D. L. Zhou, H. Wang, W. Xu, X. Chen, T. X. Zhang and H. W. Song, *RSC Adv.*, 2016, **6**, 89.
4 V. K. Tikhomirov, T. Vosch, E. Fron, V. D. Rodríguez, J. J. Velázquez, D. Kirilenko, G. Van Tendeloo, J. Hofkens, M. Van der Auweraer and V. V. Moshchalkov, *RSC Adv.*, 2012, **2**, 1496–1501.
5 A. P. Carmo, M. J. V. Bell, Z. M. D. Costa, V. Anjos, L. C. Barbosa, E. F. Chillcce, J. M. Giehl and W. M. Pontuschka, *Opt. Mater.*, 2011, **33**, 1995–1998.
6 X. H. Xu, W. F. Zhang, L. M. Jin, J. B. Qiu and S. F. Yu, *Nanoscale*, 2015, **7**, 16246.
7 L. R. P. Kassab, D. M. Silva, J. A. M. Garcia, D. S. da Silva and C. B. de Araújo, *Opt. Mater.*, 2016, **60**, 25–29.
8 B. Huang, Y. X. Zhou, P. Cheng, Z. Zhou, J. Li and W. Jin, *Opt. Mater.*, 2016, **60**, 341–349.
9 I. Soltani, S. Hraiech, K. Horchani-Naifer, H. Elhouichet, B. Gelloz and M. Férid, *J. Alloys Compd.*, 2016, **686**, 556–563.
10 F. Huang, J. C. Zhou, J. Xu and Y. S. Wang, *Nanoscale*, 2014, **6**, 2340–2344.
11 E. Malchukova, B. Boizot, G. Petite and D. Ghaleb, *J. Lumin.*, 2005, **111**, 53–59.
12 T. A. de Assumpcao, D. M. da Silva, M. E. Camilo, L. R. Kassab, A. S. Gomes, C. B. de Araújo and N. U. Wetter, *J. Alloys Compd.*, 2012, **536**, S504–S506.
13 R. K. Verma, K. Kumar and S. B. Rai, *Solid State Commun.*, 2010, **150**, 1947–1950.
14 Y. Ohko, T. Tatsuma, T. Fujii, K. Naoi, C. Niwa and Y. Kubota, *Nat. Mater.*, 2003, **2**, 29–31.
15 G. H. Silva, D. P. A. Holgado, V. Anjos, M. J. V. Bell, L. R. P. Kassab, C. T. Amâncio and R. Moncorgè, *Opt. Mater.*, 2014, **37**, 281–286.
16 Q. R. Wang, F. Song, S. X. Lin, C. G. Ming, H. Y. Zhao, J. D. Liu, C. Zhang and E. Y. B. Pun, *J. Nanopart. Res.*, 2011, **13**, 3861–3865.
17 L. Bolundut, E. Culea, G. Borodi, R. Stefan, C. Munteanu and P. Pascuta, *Ceram. Int.*, 2015, **41**, 2931–2939.
18 V. A. G. Rivera, Y. Ledemi, S. P. A. Osorio, D. Manzani, Y. Messaddeq, L. A. O. Nunes and E. Marega Jr, *J. Non-Cryst. Solids*, 2012, **358**, 399–405.
19 S. Q. Xu, Z. M. Yang, G. N. Wang, J. J. Zhang, S. X. Dai, L. L. Hu and Z. H. Jiang, *Spectrochim. Acta, Part A*, 2004, **60**, 3025–3028.
20 L. M. S. El-Deen, M. S. A. Salhi and M. M. Elkholy, *J. Alloys Compd.*, 2008, **465**, 333–339.
21 B. Klimesz, W. Ryba-Romanowski and R. Lisiecki, *Opt. Mater.*, 2015, **42**, 538–543.
22 M. R. Hasan, M. I. Hasan and M. S. Anower, *Appl. Opt.*, 2015, **54**, 9456–9461.
23 Y. M. Yang, Z. P. Yang, P. L. Li, X. Li, Q. L. Guo and B. J. Chen, *Opt. Mater.*, 2009, **32**, 133–138.
24 L. Bolundut, E. Culea, G. Borodi, R. Stefan, C. Munteanu and P. Pascuta, *Ceram. Int.*, 2015, **41**, 2931–2939.
25 V. K. Rai, L. S. Menezes, C. B. de Araújo, L. R. P. Kassab, D. M. da Silva and R. A. Kobayashi, *J. Appl. Phys.*, 2008, **103**, 093526.
26 M. Venkateswarlu, M. Prasad, K. Swapna, S. Mahamuda, A. S. Rao, A. M. Babu and D. Haranath, *Ceram. Int.*, 2014, **40**, 6261–6269.
27 V. K. Rai, C. B. de Araujo, Y. Ledemi, B. Bureau, M. Poulain, X. H. Zhang and Y. Messaddeq, *J. Appl. Phys.*, 2008, **103**, 103526.
28 G. Lakshminarayana, K. M. Kaky, S. O. Baki, S. Ye, A. Lira, I. V. Kityk and M. A. Mahdi, *J. Alloys Compd.*, 2016, **686**, 769–784.
29 S. K. Singh, N. K. Giri, D. K. Rai and S. B. Ra, *Solid State Sci.*, 2010, **12**, 1480–1483.
30 Y. W. Qi, Y. X. Zhou, L. B. Wu, F. J. Yang, S. X. Peng, S. C. Zheng and D. D. Yin, *J. Lumin.*, 2014, **153**, 40.
31 L. Bolundut, E. Culea, G. Borodi, R. Stefan, C. Munteanu and P. Pascuta, *Ceram. Int.*, 2015, **41**, 2931–2939.
32 G. V. Rao and H. D. Shashikala, *J. Non-Cryst. Solids*, 2014, **402**, 204–209.
33 S. K. Singh, N. K. Giri, D. K. Rai and S. B. Rai, *Solid State Sci.*, 2010, **12**, 1480–1483.
34 M. R. Dousti, M. R. Sahar, M. S. Rohani, A. Samavati, Z. A. Mahraz, R. J. Amjad, A. Awang and R. Arifin, *J. Mol. Struct.*, 2014, **1065–1066**, 39–42.
35 R. Driben, A. Husakou and J. Herrmann, *Opt. Express*, 2009, **17**, 17989–17995.
36 S. P. Singh and B. Karmakar, *Opt. Mater.*, 2011, **33**, 1760–1765.
37 Y. W. Qi, Y. X. Zhou, L. B. Wu, F. J. Yang, S. X. Peng, S. C. Zheng and D. D. Yin, *J. Lumin.*, 2014, **153**, 40.
38 H. Fares, H. Elhouichet, B. Gelloz and M. Férid, *J. Appl. Phys.*, 2014, **116**, 123504.
39 T. Som and B. Karmakar, *Plasmonics*, 2010, **5**, 149–159.
40 H. Tao, Y. Y. Lin, J. L. Yan and J. W. Di, *Electrochem. Commun.*, 2014, **40**, 75–79.
41 D. S. da Silva, T. A. A. de Assumpção, L. R. P. Kassab and C. B. de Araújo, *J. Alloys Compd.*, 2014, **586**, S516–S519.
42 C. B. de Araújo, T. R. Oliveira, E. L. Falcão-Filho, D. M. Silva and L. R. P. Kassab, *J. Lumin.*, 2013, **133**, 180–183.
43 J. J. Li, R. F. Wei, X. Y. Liu and H. Guo, *Opt. Express*, 2012, **20**, 10122–10127.
44 K. Annapurna, R. Chakrabarti and S. Buddhudu, *J. Mater. Sci.*, 2007, **42**, 6755–6761.
45 L. R. P. Kassab, C. B. de Araújo, R. A. Kobayashi, R. de Almeida Pinto and D. M. da Silva, *J. Appl. Phys.*, 2007, **102**, 103515.
46 B. Zhou, L. Tao, Y. H. Tsang, W. Jin and E. Y. B. Pun, *Opt. Express*, 2012, **20**, 3803–3813.
47 L. L. Zhang, G. P. Dong, M. Y. Peng and J. R. Qiu, *Spectrochim. Acta, Part A*, 2012, **93**, 223–227.
48 Y. Y. Ma, Y. Y. Guo, F. F. Huang, Y. P. Peng, L. L. Hu and J. J. Zhang, *J. Non-Cryst. Solids*, 2013, **369**, 23–28.

49 B. Huang, Y. X. Zhou, P. Cheng, Z. Z. Zhou, J. Li and G. B. Yang, *J. Alloys Compd.*, 2016, **686**, 785–792.
50 M. J. Berg, *J. Quant. Spectrosc. Radiat. Transfer*, 2012, **113**, 198.
51 E. A. Carvalho, A. P. Carmo, M. J. V. Bell, V. Anjos, L. R. P. Kassab and D. M. da Silva, *Thin Solid Films*, 2012, **520**, 2667–2671.
52 J. Massera, A. Martin, J. Choi, T. Anderson, L. Petit, M. Richardson, Y. Obeng and K. Richardson, *J. Phys. Chem. Solids*, 2010, **71**, 1634–1638.
53 A. Tarafder, A. R. Molla, S. Mukhopadhyay and B. Karmakar, *Solid State Sci.*, 2014, **37**, 144–153.
54 R. J. Amjad, M. R. Dousti and M. R. Sahar, *Curr. Appl. Phys.*, 2015, **15**, 1–7.
55 B. R. Judd, *Phys. Rev.*, 1962, **127**, 750–761.
56 G. S. Ofelt, *J. Chem. Phys.*, 1962, **37**, 511–520.
57 M. R. Rahimi, G. J. Yun, G. L. Doll and J. S. Choi, *Opt. Lett.*, 2013, **38**, 4134–4137.
58 L. L. Zhang, J. H. Zhang, X. Zhang, Z. D. Hao, G. H. Pan and H. J. Wu, *J. Lumin.*, 2016, **180**, 158–162.
59 K. Ozga, I. V. Kityk, M. Reben, J. Wasylak, N. Al Zayed, P. Rakus, A. Ślęzaka, M. Szota, M. Nabialek and M. Dospial, *J. Alloys Compd.*, 2012, **536**, S469–S471.
60 M. Reben, J. Wasylak, N. S. Alzayed, A. M. El-Naggar, M. G. Brik and I. V. Kityk, *J. Mater. Sci.: Mater. Electron.*, 2012, **23**, 631–634.